

# Band gap anomaly and topological properties in lead chalcogenides

Simin Nie,<sup>1</sup> Xiao Yan Xu,<sup>1</sup> Gang Xu,<sup>1,\*</sup> and Zhong Fang<sup>1,2</sup>

<sup>1</sup>*Beijing National Laboratory for Condensed Matter Physics, and Institute of Physics, Chinese Academy of Sciences, Beijing 100190, China*  
<sup>2</sup>*Collaborative Innovation Center of Quantum Matter, Beijing, 100084, China*

(Dated: October 24, 2018)

Band gap anomaly is a well-known issue in lead chalcogenides PbX (X=S, Se, Te, Po). Combining *ab initio* calculations and tight-binding (TB) method, we have studied the band evolution in PbX, and found that the band gap anomaly in PbTe is mainly related to the high onsite energy of Te 5s orbital and the large *s-p* hopping originated from the irregular extended distribution of Te 5s electrons. Furthermore, our calculations show that PbPo is an indirect band gap (6.5 meV) semiconductor with band inversion at L point, which clearly indicates that PbPo is a topological crystalline insulator (TCI). The calculated mirror Chern number and surface states double confirm this conclusion.

PACS numbers: 71.20.-b, 73.43.-f, 71.70.Ej

## I. INTRODUCTION

Rock-salt chalcogenides represent a significant group of functional materials, in which many novel properties are discovered, including superconductivity<sup>1</sup>, thermoelectricity<sup>2,3</sup>, ferroelectricity<sup>4</sup>, optoelectronics<sup>5,6</sup> and spintronics<sup>7,8</sup>. Recently, this class of materials has attracted considerable attention again due to the realization of the nontrivial topological properties, so called TCI<sup>9,10</sup>, in SnTe<sup>11,12</sup>. In contrast to the widely studied  $Z_2$  topological insulator (TI)<sup>13–20</sup>, Dirac cones lying on the TCI surfaces are protected by the mirror symmetry, rather than time reversal (TR) symmetry. Therefore, TCI phase is associated with a new topological invariant called mirror Chern number, which classifies and distinguishes TCI from TI and an ordinary insulator. Importantly, a quantized  $\pi$ -Berry phase induced by the band inversion is needed and essential in TCI to characterize its topological properties such as Dirac cones.

Though the discovery of TCI enriches people's understanding of the topological classification, few TCIs are realized in experiment. In order to satisfy the requirement of the potential device applications, it is urgent to find more TCIs, especially those with large band gap and high working temperature. As we all know, most lead chalcogenides adopt the same structure as SnTe, where the band inversion at L point is driven by the spin-orbit coupling (SOC). Considering that lead is much heavier than tin, it is natural to postulate that PbX may be large band gap TCI due to the much stronger SOC. However, until now, no TCI phase is realized in PbX. Therefore, it is important to figure out the main factors of the band gap evolution in rock-salt chalcogenides with the purpose of achieving large band gap TCIs. Based on previous studies, there is a famous empirical relation<sup>21</sup> between band gap  $E_G$  and lattice constant  $a_0$ , which states that  $E_G = E(L_6^-) - E(L_6^+)$  has a linear relationship with  $1/a_0^2$  for a series of relevant rock-salt semiconductors. However, this relation is invalid in lead chalcogenides, where PbTe exhibits a well-known anomaly that  $E_G(\text{PbS}) > E_G(\text{PbTe}) > E_G(\text{PbSe})$ <sup>22,23</sup>, even though the lattice constant  $a_0(\text{PbTe})$  is much larger than  $a_0(\text{PbSe})$ . This band gap anomaly has been a long-standing question and re-

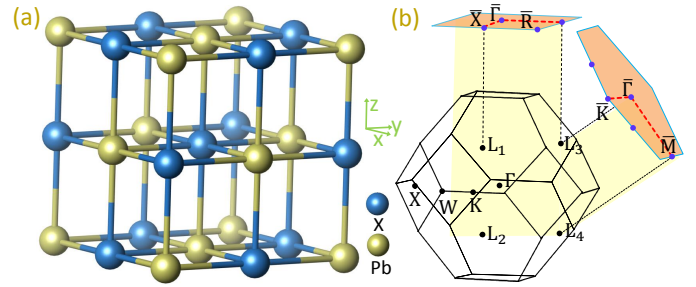


FIG. 1. (color online) (a) The crystal structure of PbX with space group  $Fm\bar{3}m$ . (b) First Brillouin zone (BZ) of bulk and the projected surface BZ on (001) and (111) planes. There are four L points ( $L_1, L_2, L_3, L_4$ ) in the bulk first BZ. For the (001) face,  $L_1$  and  $L_2$  are projected to the  $\bar{X}$ , while  $L_3$  and  $L_4$  are projected to another  $\bar{X}$ . For the (111) face,  $L_3$  is projected to  $\bar{\Gamma}$ , while  $L_1, L_2$  and  $L_4$  are projected to  $\bar{M}$ . The light yellow region is invariant under the mirror symmetry  $\hat{m}_{(1\bar{1}0)}$ .

mains under debate.

In this paper, by combining *ab initio* calculations and TB method, we have studied the band evolution and band gap anomaly in PbX. Our studies show that the band gap anomaly in PbTe is related to the delocalized 5s electrons of Te tightly. Comparing to S and Se, the 5s electrons of Te show much low binding energy (high onsite energy) and very extended distribution caused by the huge screening effect of the numerous of interior electrons. As a result, Te 5s orbital pushes up the Pb *p* orbital through the huge *s-p* hybridization, leading to a large band gap for PbTe. Moreover, our calculations show that  $E_G(\text{PbPo})$  roughly agrees with the linear relation  $E_G \propto 1/a_0^2$  formed by PbS and PbSe, and it becomes a negative number, which means that band inversion happens at L point in PbPo. Our detailed Non-local Heyd-Scuseria-Ernzerhof (HSE) hybrid functional calculations show that PbPo is an indirect band gap semiconductor with a quantized  $\pi$ -Berry phase, which clearly indicates that PbPo is a TCI. The calculated mirror Chern number and surface states double confirm this conclusion.

This paper is arranged as follows. In section II we will in-

roduce the details of the *ab initio* calculations and TB model. In section III, based on the TB model, we will study the origin of the band gap anomaly. In section IV we will focus on the electronic structure and topological properties of PbPo. Finally, section V contains a summary of this work.

## II. AB INITIO CALCULATIONS AND TB METHOD

Our *ab initio* calculations are carried out by the projector augmented wave (PAW) method<sup>24,25</sup> implemented in Vienna *ab initio* simulation package (VASP)<sup>26,27</sup>. Experimental lattice constants, with  $a_0 = 5.942$ <sup>28</sup>,  $6.124$ <sup>29</sup>,  $6.460$ <sup>30</sup>, and  $6.59$  Å<sup>31</sup> for PbS, PbSe, PbTe, and PbPo are adopted in our calculations. The exchange and correlation potential is treated within the generalized gradient approximation (GGA) of Perdew-Burke-Ernzerhof type<sup>32</sup>. Considering the possible underestimation of the band gap by GGA, HSE hybrid functional<sup>33</sup> is further supplemented to improve the accuracy of the band gap. The cutoff energy of the plane wave expansion is 500 eV, and  $11 \times 11 \times 11$  k-point grids are used in the self-consistent calculations. SOC is consistently considered in the calculations. Modified Becke-Johnson (mBJ)<sup>34</sup> calculations are performed using the all-electron full-potential linearized augmented plane-wave (FP-LAPW) method implemented in the WIEN2k package<sup>35</sup>.

In order to study the band evolution and the band gap anomaly accurately, a general eight-band Slater-Koster<sup>36</sup> TB model with bases  $\{s^C, p_x^C, p_y^C, p_z^C, s^A, p_x^A, p_y^A, p_z^A\}$  are constructed, in which, besides the  $p$ - $p$  hoppings, the  $s$ - $p$  hybridizations are taken into account too:

$$H(\mathbf{k}) = H_0(\mathbf{k}) + H_{so}(\mathbf{k}) = \begin{pmatrix} H_0^{CC}(\uparrow\uparrow) + \frac{1}{2}\xi^C L_z & H_0^{CA}(\uparrow\uparrow) & H_0^{CC}(\uparrow\downarrow) + \frac{1}{2}\xi^C L_- & H_0^{CA}(\uparrow\downarrow) \\ H_0^{AC}(\uparrow\uparrow) & H_0^{AA}(\uparrow\uparrow) + \frac{1}{2}\xi^A L_z & H_0^{AC}(\uparrow\downarrow) & H_0^{AA}(\uparrow\downarrow) + \frac{1}{2}\xi^A L_- \\ H_0^{CC}(\downarrow\uparrow) + \frac{1}{2}\xi^C L_+ & H_0^{CA}(\downarrow\uparrow) & H_0^{CC}(\downarrow\downarrow) - \frac{1}{2}\xi^C L_z & H_0^{CA}(\downarrow\downarrow) \\ H_0^{AC}(\downarrow\uparrow) & H_0^{AA}(\downarrow\uparrow) + \frac{1}{2}\xi^A L_+ & H_0^{AC}(\downarrow\downarrow) & H_0^{AA}(\downarrow\downarrow) - \frac{1}{2}\xi^A L_z \end{pmatrix} \quad (4)$$

where  $L_{\pm} = L_x \pm iL_y$ .  $L_{x,y,z}$  are the angular momentum operators.  $\xi^C$  ( $\xi^A$ ) is the SOC parameter for cation (anion)  $p$  orbital. The typical literature SOC parameters  $\xi^{Pb}=0.91$  eV,  $\xi^S=0.05$  eV,  $\xi^{Se}=0.22$  eV,  $\xi^{Te}=0.49$  eV and  $\xi^{Po}=1.06$  eV are adopted from Wittel's spectral data<sup>38</sup> in this paper.

## III. BAND GAP ANOMALY IN PbX

The band gaps calculated by different methods for PbX are shown in Fig. 3(a), in which the non-SOC band gap is defined as  $\Delta E = E(L_2^-) - E(L_1^+)$  as shown in Fig. 2(a). In Fig. 3(a),

$$H_0 = \sum_{\mu\nu} \sum_{\alpha\beta} \sum_{ij} (t_{\mu\nu,ij}^{\alpha\beta} + \varepsilon_{\mu}^{\alpha} \delta_{\mu\nu} \delta_{\alpha\beta} \delta_{ij}) c_{\mu\alpha}^+(i) c_{\nu\beta}(j) \quad (1)$$

where  $\mu, \nu =$  cation, anion label the sublattices.  $\alpha, \beta$  label the  $s, p_x, p_y$  and  $p_z$  orbitals.  $i, j$  label the atomic sites.  $t_{\mu\nu,ij}^{\alpha\beta}$  represents the corresponding hopping parameters.  $\varepsilon_{\mu}^{\alpha}$  means the onsite energy of  $\alpha$  orbital on  $\mu$  sublattice.  $c_{\mu\alpha}^+(i)$  ( $c_{\nu\beta}(j)$ ) creates (annihilates) an  $\alpha$  ( $\beta$ ) electron on  $\mu$  ( $\nu$ ) sublattice at site  $i$  ( $j$ ). The interactions up to the fourth-nearest neighbors have been considered in this paper, which leads to totally 32 independent parameters as listed in Table I. We note that all parameters in Table I are reliable and very close to previous study<sup>37</sup>. In momentum space, the Hamiltonian is given by,

$$H_0 = \sum_{\mathbf{k}} \Psi_{\mathbf{k}}^{\dagger} H_0(\mathbf{k}) \Psi_{\mathbf{k}} \quad (2)$$

with

$$H_0(\mathbf{k}) = \begin{pmatrix} H_0^{CC} & H_0^{CA} \\ H_0^{AC} & H_0^{AA} \end{pmatrix} = \begin{pmatrix} H_{1,1} & G_{1,2} & G_{1,3} & G_{1,4} & H_{1,5} & G_{1,6} & G_{1,7} & G_{1,8} \\ G_{2,1} & H_{2,2} & H_{2,3} & H_{2,4} & G_{2,5} & H_{2,6} & H_{2,7} & H_{2,8} \\ G_{3,1} & H_{3,2} & H_{3,3} & H_{3,4} & G_{3,5} & H_{3,6} & H_{3,7} & H_{3,8} \\ G_{4,1} & H_{4,2} & H_{4,3} & H_{4,4} & G_{4,5} & H_{4,6} & H_{4,7} & H_{4,8} \\ H_{5,1} & G_{5,2} & G_{5,3} & G_{5,4} & H_{5,5} & G_{5,6} & G_{5,7} & G_{5,8} \\ G_{6,1} & H_{6,2} & H_{6,3} & H_{6,4} & G_{6,5} & H_{6,6} & H_{6,7} & H_{6,8} \\ G_{7,1} & H_{7,2} & H_{7,3} & H_{7,4} & G_{7,5} & H_{7,6} & H_{7,7} & H_{7,8} \\ G_{8,1} & H_{8,2} & H_{8,3} & H_{8,4} & G_{8,5} & H_{8,6} & H_{8,7} & H_{8,8} \end{pmatrix} \quad (3)$$

where  $H_{i,j}$  and  $G_{i,j}$  mean the matrix elements are real and imaginary, respectively. The detailed descriptions of all matrix elements are given in the Appendix.

When SOC is taken into account, the Hamiltonian size will be doubled. The final Hamiltonian with SOC can be written in the form,

the band gaps for PbTe show a distinct jump in all calculation methods, which means the band gap anomaly in PbTe is intrinsic of the material, and irrelevant to SOC and the form of the exchange-correlation functional. Comparing all the results shown in Fig. 3(a), we find HSE03+SOC is the most superior method, which gives almost the same band gaps as the experimental measurements for all materials. Therefore, in the following, the band structures calculated by HSE03 without SOC are taken as reference to fit the parameters in Eq. (3), and all parameters are directly transferred to Eq. (4) by adding the isotropic SOC term to estimate the band gaps and dispersions for all compounds. The comparisons between the

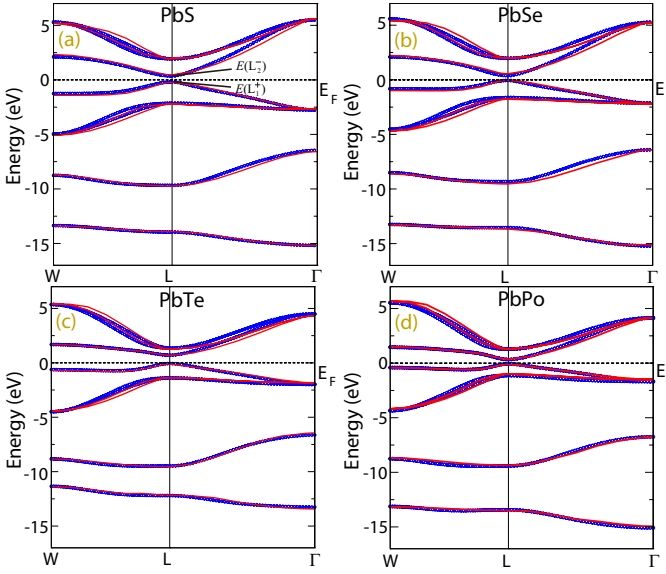


FIG. 2. (color online) Non-SOC band structures of PbX. The red lines and the blue dots are obtained from HSE03 calculations and TB model fitting respectively.

non-SOC band structures obtained by Eq. (3) and original HSE03 calculations are shown in Fig. 2, and all fitted parameters are listed in Table I, in which the detailed definitions of them are given in the six and seven columns. Taking  $D_3$  as an example, “ $x, s(100)$ ” and “ $C-A$ ” mean  $D_3$  is the hopping parameter from the  $p_x$  orbital ( $x$ ) of cation ( $C$ ) to the  $s$  orbital ( $s$ ) of anion ( $A$ ) along the vector  $a_0/2$  (1,0,0). In Fig. 2, the non-SOC band structures obtained from HSE03 calculations and TB fittings by Eq. (3) are plotted with red lines and blue dots respectively. It is clear that our TB results agree with HSE03 calculations very well, which certifies that our model is accurate enough to study all details of the system.

The estimated band gaps  $E_G$  (red circles) from Eq. (4) for all four compounds, as well as the experimental data at 4.2 K (blue pentagons), are summarized in Fig. 3(b). It is clear that our TB results overlap with the experimental data almost, which certifies that our model is accurate and powerful again. In order to study the origin of the band gap anomaly in PbTe, we have checked all the parameters in Table I carefully and found that the  $s$  orbital onsite energy of Te ( $C_1$ ) is obviously higher than the other three. Taking  $A_1$  (onsite energy of cation  $s$  orbital) as a referential energy, we get  $C_1-A_1$  equal to -5.7716, -5.8421, -3.4233 and -5.3128 for PbS, PbSe, PbTe and PbPo respectively. As a result, the band energy of Te 5s orbital at  $\Gamma$  point shown in Fig. 2(c) is about -13 eV, while it is nearly -15 eV for the other three compounds. Owing to this high onsite energy, Te 5s orbital will push up Pb 6p orbital through the  $s-p$  hybridization and result in a large band gap for PbTe. Now, we try to artificially decrease the onsite energy of Te 5s orbital and push down the band energy at  $\Gamma$  point until it reaches the “regular” level -15 eV as the other three. (For this purpose,  $C_1$  needs to be decreased by 2 eV.) After this adjustment, though the band gap does decrease about 0.2 eV as shown as the green triangle in Fig. 3(b), the band gap

TABLE I. Fitted TB parameters (in eV).

	PbS	PbSe	PbTe	PbPo		
$A_1$	-1.1333	-2.0072	-1.6603	-2.2198	s,s(000)	C-C
$A_2$	0.0991	0.0891	0.0959	0.0857	s,s(110)	C-C
$A_3$	-0.0012	-0.0215	-0.0406	-0.0623	s,x(110)	C-C
$A_6$	7.7801	6.9910	7.2422	6.7530	x,x(000)	C-C
$A_7$	-0.0002	-0.0259	-0.0574	-0.0830	x,x(110)	C-C
$A_8$	-0.0169	-0.0283	-0.0419	-0.0535	x,x(011)	C-C
$A_9$	0.3623	0.3110	0.2693	0.2157	x,y(110)	C-C
$C_1$	-6.9050	-7.8493	-5.0836	-7.5326	s,s(000)	A-A
$C_2$	-0.0793	-0.0848	-0.0907	-0.0894	s,s(110)	A-A
$C_3$	0.1584	0.1689	0.1788	0.1875	s,x(110)	A-A
$C_6$	3.3582	3.1139	4.2744	4.2034	x,x(000)	A-A
$C_7$	0.1611	0.1686	0.1740	0.1810	x,x(110)	A-A
$C_8$	-0.0170	-0.0188	-0.0203	-0.0217	x,x(011)	A-A
$C_9$	0.1480	0.1356	0.1201	0.1106	x,y(110)	A-A
$B_1$	-0.1537	-0.1257	-0.1082	-0.0779	s,s(200)	C-C
$B_2$	0.0855	0.0974	0.1113	0.1247	s,x(200)	C-C
$B_4$	0.5301	0.4891	0.4579	0.4131	x,x(200)	C-C
$B_5$	0.1262	0.1050	0.0870	0.0605	y,y(200)	C-C
$E_1$	-0.2421	-0.2215	-0.1947	-0.1701	s,s(200)	A-A
$E_2$	-0.0854	-0.1308	-0.1733	-0.2168	s,x(200)	A-A
$E_4$	0.1210	0.1409	0.1516	0.1713	x,x(200)	A-A
$E_5$	0.0298	0.0330	0.0360	0.0393	y,y(200)	A-A
$D_1$	-0.6586	-0.6076	-0.5565	-0.5015	s,s(100)	C-A
$D_2$	1.3365	1.2714	1.2389	1.1757	s,x(100)	C-A
$D_3$	-1.6336	-1.4507	-1.4907	-1.2878	x,s(100)	C-A
$D_4$	1.8308	1.8474	1.8633	1.8795	x,x(100)	C-A
$D_5$	-0.2662	-0.2950	-0.3287	-0.3675	y,y(100)	C-A
$F_1$	0.3581	0.3100	0.2688	0.2239	s,s(111)	C-A
$F_2$	-0.0504	-0.0491	-0.0481	-0.0470	x,s(111)	C-A
$F_3$	-0.0071	-0.0069	-0.0067	-0.0065	s,x(111)	C-A
$F_4$	0.1154	0.1013	0.0868	0.0736	x,x(111)	C-A
$F_5$	0.0315	0.0425	0.0564	0.0680	x,y(111)	C-A

anomaly is still evident. Therefore, there must be some other reasons responsible to the band gap anomaly in addition to the high onsite energy of Te 5s orbital. We then recheck all the parameters in Table I, and find that  $D_3$  also show some irregularity. Naturally,  $|D_3|$  should decrease monotonically from PbS to PbPo due to the increasing lattice constant. However,  $|D_3(\text{PbTe})|$  is a little larger than  $|D_3(\text{PbSe})|$ , even though  $a_0(\text{PbTe}) = 6.460 \text{ \AA}$  is obviously larger than  $a_0(\text{PbSe}) = 6.124 \text{ \AA}$ . Based on the above discussions, after decreasing  $C_1$  by 2 eV and increasing  $D_3$  by 0.08 eV to a “regular” number, the final band gap for PbTe is shown as the purple square in Fig. 3(b), which falls on the line formed by PbS-PbSe-PbPo almost. Therefore, we conclude that the band gap anomaly in PbTe is mainly related to the high onsite energy of Te 5s orbital and the irregularly large  $s-p$  hopping.

Because SOC nearly has no contribution to the band gap anomaly as identified by our *ab initio* calculations, we would like to analytically discuss the band gap evolution and anomaly based on the non-SOC TB model in the following. At this case, the band gap  $\Delta E$  can be easily written as:

$$\Delta E = \frac{1}{2} [A_6 - 8A_9 - 6E_1 - 4B_5 - 2B_4 + C_1 + \sqrt{48D_3^2 + (A_6 - 8A_9 + 6E_1 - 4B_5 - 2B_4 - C_1)^2} - (A_1 - 8C_9 - 6B_1 - 4E_5 - 2E_4 + C_6 + \sqrt{48D_3^2 + (-A_1 - 8C_9 + 6B_1 - 4E_5 - 2E_4 + C_6)^2})] \quad (5)$$

which shows an explicit relation between  $\Delta E$ ,  $C_1$  and  $D_3$ . In

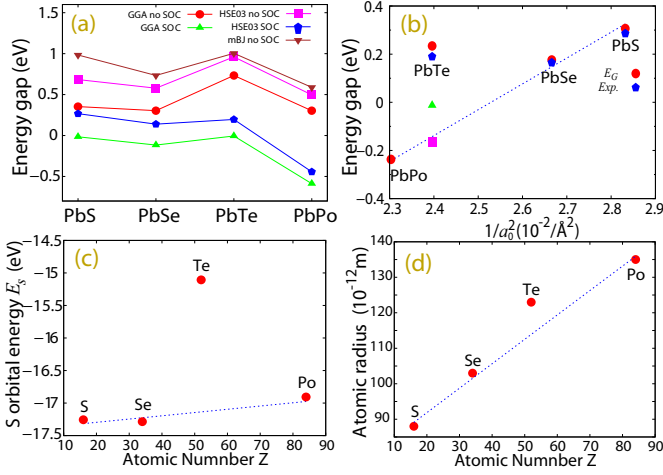


FIG. 3. (color online) (a) Band gaps  $E_G$  at L point for PbX calculated by different methods. (b) TB band gap  $E_G$  for PbX as a function of  $1/a_0^2$ . Available experimental data at 4.2 K (blue pentagons) are plotted for comparison. (c) and (d) Outermost  $s$ -electron binding energy  $E_s$  and atomic radius for S, Se, Te and Po as a function of the atomic number  $Z$ .

Eq. (5), if we omit  $D_3$ , all  $C_1$  ( $E_1$ ) terms will cancel with each other, which means that the anomaly of  $C_1$  needs the help of  $D_3$  to involve in the band gap formation and finally leads to a large gap for PbTe. Therefore, besides the directly bonded  $p$ - $p$  hopping parameters ( $A_9$ ,  $C_9$ , etc.), the key factors in determining the band gap for PbX are the huge  $s$ - $p$  hybridization  $D_3$  ( $D_2$ ) and the irregular high onsite energy  $C_1$ . We note that, such huge  $s$ - $p$  hybridization is a typical character of the covalent systems rather than the ionic compounds. Generally, the hybridizations between the bonding (antibonding) states and non-bonding states are very weak in ionic compounds, such as  $\text{CaX}$  ( $X=\text{S, Se, Te}$ ),  $\text{SrX}$  ( $X=\text{S, Se, Te}$ ) and  $\text{BaX}$  ( $X=\text{S, Se, Te}$ )<sup>39</sup>, in which the irregular high onsite energy of Te  $s$  orbital has negligible influence on the band gap  $E_G$  because the  $s$  (antibonding state from cation)- $s$  (non-bonding state from anion) hybridization is negligible. This is the main reason why  $\text{CaX}$ ,  $\text{SrX}$  and  $\text{BaX}$  all obey the empirical relation  $E_G \propto 1/a_0^2$  very well, even though the irregularity of the Te  $s$  orbital also exists in all these ionic systems. Moreover, we note that the  $s$ - $p$  hybridizations  $D_3$  ( $D_2$ ) in lead chalcogenides are too strong to be treated by the perturbation method<sup>40</sup>. Using the fitted parameters for PbTe to do a rough estimation,  $48D_3^2$  is almost equal to  $(A_6 - 8A_9 + 6E_1 - 4B_5 - 2B_4 - C_1)^2$ . Therefore, the first square root in the right hand of Eq. (5) is approximately equal to  $1/\sqrt{2}[\sqrt{48}|D_3| + (A_6 - 8A_9 + 6E_1 - 4B_5 - 2B_4 - C_1)]$ , which can be used to estimate the band gap evolution with  $C_1$  and  $D_3$  roughly.

Next, we would like to discuss the origin of the irregularity of  $C_1$  and  $D_3$  deeply. Because both  $C_1$  and  $D_3$  are related to the  $s$  orbital of anion tightly, it is natural to propose that the irregularity may be originated from the chalcogen atoms themselves. We have calculated the binding energies of the outermost  $s$  electrons  $E_s$  for all chalcogen atoms and plotted them with the atomic number  $Z$  in Fig. 3(c), in which the

points for sulfur, selenium and polonium show an approximately straight line while the point of tellurium is much higher than the straight line. This result clearly demonstrates that the high onsite energy  $C_1$  of PbTe is inherited from the low binding energy of tellurium  $5s$  electrons. To study the irregularity of  $D_3$  in PbTe, we show a plot of the atomic radius of the chalcogen atoms<sup>41</sup> as a function of atomic number  $Z$  in Fig. 3(d). We can see that the atomic radius of tellurium does not lie on the straight line as the others do and its position is higher than the line, which means tellurium  $5s$  orbital is more extended. As a result, the hybridization between  $5s$  orbital of Te and  $p_x$  orbital of Pb, *i.e.*  $D_3$ , is abnormally larger than the “regular” value. Both the low binding energy and the extended distribution of the tellurium  $5s$  electrons are related to the unusually strong screening effect of the V-period elements, as well as the penetration effect and relativistic effect. In general, the huge screening effect from the interior electrons will reduce the binding effect of nucleus and lead to a low binding energy and more extended distribution of Te  $5s$  electrons. However, the detailed discussions of the atomic energy level and distribution are very complicated and out of the scope of this work. Finally, we claim that such  $5s$  electrons irregularity is universal for the right side elements in the V row of the periodic Table of Elements<sup>42</sup>, *e.g.* Sn, and our discussion is universal for other covalent systems with the same structure. For example, similar analysis would give the conclusion that the  $5s$  orbital irregularity of Sn will obviously reduce the band gap of the tin chalcogenides, which may be the main reason why the band gap of tin chalcogenide is usually smaller than the same row lead chalcogenide<sup>43,44</sup>.

#### IV. TOPOLOGICAL PROPERTIES IN PbPo

One important result of our calculations is that  $E_G$  is negative for PbPo as shown in Fig. 3(b), which means that band inversion happens at L point of PbPo. Detailed HSE03+SOC calculations have been performed to confirm this conclusion. The calculated band structure is shown in Fig. 4(a), in which one  $p$  orbital of Pb is obviously dropped down below the Fermi level at L point as represented by the blue circles. Furthermore, our calculations show that PbPo is an indirect band gap (6.5 meV) semiconductor (see inset of Fig. 4(a)), rather than a direct band gap semiconductor<sup>45</sup> or semimetal<sup>46</sup>. All these band characters of PbPo are very similar to SnTe, which implies that PbPo may be a TCI too.

There are four L points  $\{L_1(0, \pi, 0), L_2(0, 0, \pi), L_3(\pi, \pi, \pi), L_4(\pi, 0, 0)\}$  in the first BZ of PbPo (see Fig. 1(b)). Because there are even band inversion points, the topological property of PbPo is different with 3D strong TI<sup>47,48</sup>. Actually, the topological property is protected by the mirror symmetry, and its topological invariant is the mirror Chern number  $C_M$  instead of  $Z_2$ .

The eigenvalue ( $m$ ) of the mirror operator  $\hat{m}_{(1\bar{1}0)}$  is a good quantum number for PbPo. So we can classify the Bloch wavefunctions on  $(1\bar{1}0)$  plane by  $m$ , and define the berry connection  $\mathbf{A}^m(\mathbf{k})$  and berry curvature  $\Omega^m(\mathbf{k})$  on the plane as fol-

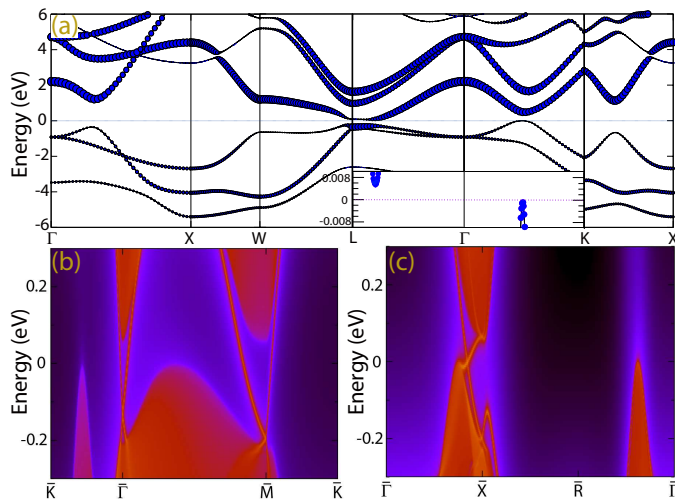


FIG. 4. (color online) (a) Band structures of PbPo calculated by HSE03+SOC. The size of the blue circles represents the weight of the projected  $p$  orbitals of Pb. The inset shows the top of the valence band and the bottom of the conduction band of PbPo. (b) and (c) The calculated surface states on (111) and (001) planes.

lows:

$$\mathbf{A}^m(\mathbf{k}) = i \sum_n \langle u_n^m(\mathbf{k}) | \nabla_{\mathbf{k}} | u_n^m(\mathbf{k}) \rangle \quad (6)$$

$$\Omega^m(\mathbf{k}) = \nabla_{\mathbf{k}} \times \mathbf{A}^m(\mathbf{k}) \quad (7)$$

where  $u_n^m(\mathbf{k})$  with mirror eigenvalue  $m = \pm i$  is the  $n$ th eigenstate at  $\mathbf{k}$  point. The sum is over all occupied bands. The mirror Chern number  $C_M$  is defined as  $C_M = (n_{+i} - n_{-i})/2$ , where  $n_m = \int \Omega^m(\mathbf{k}) \cdot d\mathbf{S}$ . Using above formula, we find  $C_M = -2$  for PbPo, which confirms that PbPo is a TCI. The other hallmark of the TCI is the mirror symmetry protected nontrivial surface states. We have calculated the surface states on (111) and (001) plane as shown in Fig. 4(b) and Fig. 4(c), respectively. As we can see, there are two distinct Dirac cones: one is pinned at the time reversal invariant momentum (TRIM)

point while the other is situated off the TRIM point. On (111) plane,  $L_2$ ,  $L_3$  and  $L_4$  are projected to the same point  $\bar{M}$ , while  $L_1$  is projected to  $\bar{\Gamma}$  point. There is no additional interaction coming from the scattering between odd L-valleys. So the Dirac cones on (111) plane exactly locate at the TRIM points as shown in Fig. 4(b). On (001) plane,  $L_1$  and  $L_2$  ( $L_3$  and  $L_4$ ) are projected to the same point  $\bar{X}$  (another  $\bar{X}$ ). The interaction between two L-valleys will introduce an additional term to push the Dirac cones away from TRIM point<sup>49</sup>. However,  $k$ -points along  $\bar{\Gamma} - \bar{X}$  direction preserve mirror symmetry with respect  $\hat{m}_{(1\bar{1}0)}$  operator. Therefore, even the Dirac cones are pushed away from TRIM point, they can still survive along  $\bar{\Gamma} - \bar{X}$  direction as shown in Fig. 4(c). The Dirac cones are protected by the mirror symmetry rather than TR symmetry, which is an important difference between TCI and  $Z_2$  TI.

## V. CONCLUSION

In summary, we have studied the band evolution in PbX, and found that, though the  $s$  orbital of the anion is far away from the Fermi level, it has crucial influence on the band gap through the huge  $s$ - $p$  hybridization. The high onsite energy of Te  $s$  orbital and its irregular extended distribution combining together result in an irregular big band gap in PbTe, *i.e.* the famous band gap anomaly in lead chalcogenides. Furthermore, our calculations show that PbPo is an indirect band gap (6.5 meV) semiconductor with negative  $E_G$ , which means that band inversion happens at L point in PbPo. The calculated mirror Chern number and surface states confirm that PbPo is a TCI.

## ACKNOWLEDGMENTS

We thank Xianxin Wu, Zhijun Wang, Richard Martin and Theodore Geballe for valuable discussions, the support from National Science Foundation of China (Grant Nos. 11204359), the 973 program of China (Grant Nos. 2013CB921700), and the Strategic Priority Research Program (B) of the Chinese Academy of Sciences (Grant Nos. XDB07020100).

\* gangx@iphy.ac.cn

<sup>1</sup> Y. Matsushita, P. Wiannecki, A. T. Sommer, T. Geballe, and I. Fisher, *Physical Review B* **74**, 134512 (2006).

<sup>2</sup> C. Wood, *Reports on progress in physics* **51**, 459 (1988).

<sup>3</sup> H. Wang, Y. Pei, A. D. LaLonde, and G. J. Snyder, *Advanced Materials* **23**, 1366 (2011).

<sup>4</sup> A. I. Lebedev and I. A. Sluchinskaya, *Ferroelectrics* **157**, 275 (1994).

<sup>5</sup> B. . A. Akimov, A. Dmitriev, D. Khokhlov, and L. Ryabova, *physica status solidi (a)* **137**, 9 (1993).

<sup>6</sup> Y. Liu, M. Gibbs, J. Puthussery, S. Gaik, R. Ihly, H. W. Hillhouse, and M. Law, *Nano letters* **10**, 1960 (2010).

<sup>7</sup> S. Jin, H. Wu, and T. Xu, *Applied Physics Letters* **95**, 132105 (2009).

<sup>8</sup> G. Grabecki, *Journal of applied physics* **101**, 081722 (2007).

<sup>9</sup> L. Fu, *Physical Review Letters* **106**, 106802 (2011).

<sup>10</sup> H. Weng, J. Zhao, Z. Wang, Z. Fang, and X. Dai, *Physical review letters* **112**, 016403 (2014).

<sup>11</sup> T. H. Hsieh, H. Lin, J. Liu, W. Duan, A. Bansil, and L. Fu, *Nature communications* **3**, 982 (2012).

<sup>12</sup> Y. Tanaka, Z. Ren, T. Sato, K. Nakayama, S. Souma, T. Takahashi, K. Segawa, and Y. Ando, *Nature Physics* **8**, 800 (2012).

<sup>13</sup> M. Z. Hasan and C. L. Kane, *Reviews of Modern Physics* **82**, 3045 (2010).

<sup>14</sup> X.-L. Qi and S.-C. Zhang, *Reviews of Modern Physics* **83**, 1057 (2011).

<sup>15</sup> H. Weng, X. Dai, and Z. Fang, *MRS Bulletin* **39**, 849 (2014).

<sup>16</sup> H. Weng, X. Dai, and Z. Fang, *Physical Review X* **4**, 011002 (2014).

- 17 H. Weng, A. Ranjbar, Y. Liang, Z. Song, M. Khazaei, S. Yunoki, M. Arai, Y. Kawazoe, Z. Fang, and X. Dai, *Physical Review B* **92**, 075436 (2015).
- 18 G. Xu, H. Weng, Z. Wang, X. Dai, and Z. Fang, *Physical review letters* **107**, 186806 (2011).
- 19 G. Xu, J. Wang, C. Felser, X.-L. Qi, and S.-C. Zhang, *Nano Letters* **15**, 2019 (2015).
- 20 S. M. Nie, Z. Song, H. Weng, and Z. Fang, *Phys. Rev. B* **91**, 235434 (2015).
- 21 T. Moss, *Optical properties of semiconductors, a semiconductor monograph* (Butterworths Scientific Publications and Academic Press, London and New York, 1959).
- 22 D. Long, *Journal of Applied Physics* **33**, 1682 (1962).
- 23 R. Dalven, *Physical Review B* **3**, 3359 (1971).
- 24 P. E. Blöchl, *Physical Review B* **50**, 17953 (1994).
- 25 G. Kresse and D. Joubert, *Physical Review B* **59**, 1758 (1999).
- 26 G. Kresse and J. Furthmüller, *Computational Materials Science* **6**, 15 (1996).
- 27 G. Kresse and J. Furthmüller, *Physical Review B* **54**, 11169 (1996).
- 28 S. Mehmood, S. Zaman, K. Ahmed, and M. Asim, *Key Engineering Materials* **442**, 123 (2010).
- 29 I. Aliev, K. Babanly, and N. Babanly, *Inorganic Materials* **44**, 1179 (2008).
- 30 R. Minikayev, E. Dynowska, E. Kaminska, A. Szczerbakow, D. Trots, T. Story, and W. Szuszkiewicz, *Acta Phys. Pol. A* **119**, 699 (2011).
- 31 W. Witteman, A. Giorgi, and D. Vier, *The Journal of Physical Chemistry* **64**, 434 (1960).
- 32 J. Perdew, K. Burke, and M. Ernzerhof, *Phys. Rev. Lett.* **77**, 3865 (1996).
- 33 J. Heyd, G. E. Scuseria, and M. Ernzerhof, *The Journal of Chemical Physics* **118**, 8207 (2003).
- 34 F. Tran and P. Blaha, *Physical Review Letters* **102**, 226401 (2009).
- 35 P. Blaha, K. Schwarz, G. Madsen, D. Kvasnicka, and J. Luitz, WIEN2k, An Augmented Plane Wave Plus Local Orbitals Program for Calculating Crystal Properties (TU Vienna, Vienna, 2001).
- 36 J. C. Slater and G. F. Koster, *Physical Review* **94**, 1498 (1954).
- 37 M. Lach-Hab, M. Keegan, D. Papaconstantopoulos, and M. Mehl, *Journal of Physics and Chemistry of Solids* **61**, 1639 (2000).
- 38 K. Wittel and R. Manne, *Theoretical Chemistry Accounts: Theory, Computation, and Modeling (Theoretica Chimica Acta)* **33**, 347 (1974).
- 39 R. Dalven, *Physical Review B* **8**, 6033 (1973).
- 40 P. Barone, T. Rauch, D. Di Sante, J. Henk, I. Mertig, and S. Picozzi, *Physical Review B* **88**, 045207 (2013).
- 41 E. Clementi, D. Raimondi, and W. Reinhardt, *The Journal of chemical physics* **47**, 1300 (1967).
- 42 K. D. Sevier, *Atomic Data and Nuclear Data Tables* **24**, 323 (1979).
- 43 Y. Sun, Z. Zhong, T. Shirakawa, C. Franchini, D. Li, Y. Li, S. Yunoki, and X.-Q. Chen, *Physical Review B* **88**, 235122 (2013).
- 44 R. Tsu, W. E. Howard, and L. Esaki, *Phys. Rev.* **172**, 779 (1968).
- 45 R. Dalven, *Physical Review Letters* **28**, 91 (1972).
- 46 S. Rabii and R. Lasseter, *Phys. Rev. Lett.* **33**, 703 (1974).
- 47 H. Zhang, C.-X. Liu, X.-L. Qi, X. Dai, Z. Fang, and S.-C. Zhang, *Nature Physics* **5**, 438 (2009).
- 48 W. Zhang, R. Yu, W. Feng, Y. Yao, H. Weng, X. Dai, and Z. Fang, *Physical review letters* **106**, 156808 (2011).
- 49 J. Liu, W. Duan, and L. Fu, *Phys. Rev. B* **88**, 241303 (2013).

## APPENDIX

In the APPENDIX, the detailed descriptions of the real and imaginary matrix elements in Eq. (3) are shown in Table II and Table III respectively.

TABLE II. Real part of  $H_0(\mathbf{k})$

$H_{1,1}$	$A_1 + 4A_2[\cos(k_x)\cos(k_y) + \cos(k_y)\cos(k_z) + \cos(k_z)\cos(k_x)] + 2B_1[\cos(2k_x) + \cos(2k_y) + \cos(2k_z)]$
$H_{1,5}$	$2D_1[\cos(k_x) + \cos(k_y) + \cos(k_z)] + 8F_1\cos(k_x)\cos(k_y)\cos(k_z)$
$H_{2,2}$	$A_6 + 4A_7\cos(k_x)[\cos(k_y) + \cos(k_z)] + 4A_8\cos(k_y)\cos(k_z) + 2B_4\cos(2k_x) + 2B_5[\cos(2k_y) + \cos(2k_z)]$
$H_{2,3}$	$-4A_9\sin(k_x)\sin(k_y)$
$H_{2,4}$	$-4A_9\sin(k_x)\sin(k_z)$
$H_{2,6}$	$2D_4\cos(k_x) + 2D_5[\cos(k_y) + \cos(k_z)] + 8F_4\cos(k_x)\cos(k_y)\cos(k_z)$
$H_{2,7}$	$-8F_5\sin(k_x)\sin(k_y)\cos(k_z)$
$H_{2,8}$	$-8F_5\sin(k_x)\sin(k_z)\cos(k_y)$
$H_{3,3}$	$A_6 + 4A_7\cos(k_y)[\cos(k_z) + \cos(k_x)] + 4A_8\cos(k_z)\cos(k_x) + 2B_4\cos(2k_y) + 2B_5[\cos(2k_z) + \cos(2k_x)]$
$H_{3,4}$	$-4A_9\sin(k_y)\sin(k_z)$
$H_{3,6}$	$H_{2,7}$
$H_{3,7}$	$2D_4\cos(k_y) + 2D_5[\cos(k_z) + \cos(k_x)] + 8F_4\cos(k_x)\cos(k_y)\cos(k_z)$
$H_{3,8}$	$-8F_5\sin(k_y)\sin(k_z)\cos(k_x)$
$H_{4,4}$	$A_6 + 4A_7\cos(k_z)[\cos(k_x) + \cos(k_y)] + 4A_8\cos(k_x)\cos(k_y) + 2B_4\cos(2k_z) + 2B_5[\cos(2k_x) + \cos(2k_y)]$
$H_{4,6}$	$H_{2,8}$
$H_{4,7}$	$H_{3,8}$
$H_{4,8}$	$2D_4\cos(k_z) + 2D_5[\cos(k_y) + \cos(k_x)] + 8F_4\cos(k_x)\cos(k_y)\cos(k_z)$
$H_{5,5}$	$C_1 + 4C_2[\cos(k_x)\cos(k_y) + \cos(k_y)\cos(k_z) + \cos(k_z)\cos(k_x)] + 2E_1[\cos(2k_x) + \cos(2k_y) + \cos(2k_z)]$
$H_{6,6}$	$C_6 + 4C_7\cos(k_x)[\cos(k_y) + \cos(k_z)] + 4C_8\cos(k_y)\cos(k_z) + 2E_4\cos(2k_x) + 2E_5[\cos(2k_y) + \cos(2k_z)]$
$H_{6,7}$	$-4C_9\sin(k_x)\sin(k_y)$
$H_{6,8}$	$-4C_9\sin(k_x)\sin(k_z)$
$H_{7,7}$	$C_6 + 4C_7\cos(k_y)[\cos(k_z) + \cos(k_x)] + 4C_8\cos(k_z)\cos(k_x) + 2E_4\cos(2k_y) + 2E_5[\cos(2k_z) + \cos(2k_x)]$
$H_{7,8}$	$-4C_9\sin(k_y)\sin(k_z)$
$H_{8,8}$	$C_6 + 4C_7\cos(k_z)[\cos(k_x) + \cos(k_y)] + 4C_8\cos(k_x)\cos(k_y) + 2E_4\cos(2k_z) + 2E_5[\cos(2k_x) + \cos(2k_y)]$

TABLE III. Image part of  $H_0(\mathbf{k})$ 

$G_{1,2}$	$-4A_3 \sin(k_x) [\cos(k_y) + \cos(k_z)] - 2B_2 \sin(2k_x)$
$G_{1,3}$	$-4A_3 \sin(k_y) [\cos(k_z) + \cos(k_x)] - 2B_2 \sin(2k_y)$
$G_{1,4}$	$-4A_3 \sin(k_z) [\cos(k_x) + \cos(k_y)] - 2B_2 \sin(2k_z)$
$G_{1,6}$	$2D_2 \sin(k_x) + 8F_3 \sin(k_x) \cos(k_y) \cos(k_z)$
$G_{1,7}$	$2D_2 \sin(k_y) + 8F_3 \sin(k_y) \cos(k_z) \cos(k_x)$
$G_{1,8}$	$2D_2 \sin(k_z) + 8F_3 \sin(k_z) \cos(k_x) \cos(k_y)$
$G_{2,5}$	$-2D_3 \sin(k_x) - 8F_2 \sin(k_x) \cos(k_y) \cos(k_z)$
$G_{3,5}$	$-2D_3 \sin(k_y) - 8F_2 \sin(k_y) \cos(k_z) \cos(k_x)$
$G_{4,5}$	$-2D_3 \sin(k_z) - 8F_2 \sin(k_z) \cos(k_x) \cos(k_y)$
$G_{5,6}$	$-4C_3 \sin(k_x) [\cos(k_y) + \cos(k_z)] - 2E_2 \sin(2k_x)$
$G_{5,7}$	$-4C_3 \sin(k_y) [\cos(k_z) + \cos(k_x)] - 2E_2 \sin(2k_y)$
$G_{5,8}$	$-4C_3 \sin(k_z) [\cos(k_x) + \cos(k_y)] - 2E_2 \sin(2k_z)$